


RESEARCH

Open Access



Electrocardiogram-less, free-breathing myocardial extracellular volume fraction mapping in small animals at high heart rates using motion-resolved cardiovascular magnetic resonance multitasking: a feasibility study in a heart failure with preserved ejection fraction rat model

Pei Han^{1,2†}, Rui Zhang^{3,4†}, Shawn Wagner², Yibin Xie², Eugenio Cingolani³, Eduardo Marban³, Anthony G. Christodoulou^{1,2*} and Debiao Li^{1,2*} 

Abstract

Background: Extracellular volume fraction (ECV) quantification with cardiovascular magnetic resonance (CMR) T_1 mapping is a powerful tool for the characterization of focal or diffuse myocardial fibrosis. However, it is technically challenging to acquire high-quality T_1 and ECV maps in small animals for preclinical research because of high heart rates and high respiration rates. In this work, we developed an electrocardiogram (ECG)-less, free-breathing ECV mapping method using motion-resolved CMR Multitasking on a 9.4 T small animal CMR system. The feasibility of characterizing diffuse myocardial fibrosis was tested in a rat heart failure model with preserved ejection fraction (HFpEF).

Methods: High-salt fed rats diagnosed with HFpEF ($n=9$) and control rats ($n=9$) were imaged with the proposed ECV Multitasking technique. A 25-min exam, including two 4-min T_1 Multitasking scans before and after gadolinium injection, were performed on each rat. It allows a cardiac temporal resolution of 20 ms for a heart rate of ~ 300 bpm. Myocardial ECV was calculated from the hematocrit (HCT) and fitted T_1 values of the myocardium and the blood pool. Masson's trichrome stain was used to measure the extent of fibrosis. Welch's t-test was performed between control and HFpEF groups.

Results: ECV was significantly higher in the HFpEF group ($22.4\% \pm 2.5\%$ vs. $18.0\% \pm 2.1\%$, $P=0.0010$). A moderate correlation between the ECV and the extent of fibrosis was found ($R=0.59$, $P=0.0098$).

Conclusions: Motion-resolved ECV Multitasking CMR can quantify ECV in the rat myocardium at high heart rates without ECG triggering or respiratory gating. Elevated ECV found in the HFpEF group is consistent with previous

*Correspondence: Anthony.Christodoulou@cshs.org; Debiao.Li@cshs.org

†Pei Han and Rui Zhang contributed equally to this work

¹ Department of Bioengineering, University of California, Los Angeles, Los Angeles, CA, USA

Full list of author information is available at the end of the article



© The Author(s) 2021. **Open Access** This article is licensed under a Creative Commons Attribution 4.0 International License, which permits use, sharing, adaptation, distribution and reproduction in any medium or format, as long as you give appropriate credit to the original author(s) and the source, provide a link to the Creative Commons licence, and indicate if changes were made. The images or other third party material in this article are included in the article's Creative Commons licence, unless indicated otherwise in a credit line to the material. If material is not included in the article's Creative Commons licence and your intended use is not permitted by statutory regulation or exceeds the permitted use, you will need to obtain permission directly from the copyright holder. To view a copy of this licence, visit <http://creativecommons.org/licenses/by/4.0/>. The Creative Commons Public Domain Dedication waiver (<http://creativecommons.org/publicdomain/zero/1.0/>) applies to the data made available in this article, unless otherwise stated in a credit line to the data.

human studies and well correlated with histological data. This technique has the potential to be a viable imaging tool for myocardial tissue characterization in small animal models.

Keywords: Cardiovascular MR, T_1 mapping, Extracellular volume fraction, HFpEF

Background

Cardiovascular magnetic resonance (CMR) T_1 mapping is a powerful diagnostic modality for various abnormalities of the myocardium, such as edema, amyloidosis, and overload of lipid or iron [1–3]. Combined with gadolinium (Gd) contrast enhancement, T_1 mapping allows extracellular volume fraction (ECV) quantification, which can be used to characterize focal or diffuse myocardial fibrosis [3–6].

Rodent models are widely used in preclinical studies of myocardial diseases because of the short development period, availability of genetically modified disease models, and low cost. However, it is technically challenging to acquire high-quality T_1 and ECV maps in small animals because of their high heart rates (often >300 bpm) and high respiration rates (around 60 cpm). Therefore, CMR quantification of ECV is still not well established despite the important unmet needs in research. Several studies have been done to improve CMR T_1 mapping and/or ECV measurement in small animals. Coolen et al. proposed a 3D T_1 mapping method of the mouse heart using variable flip angle (VFA) analysis [7]. The method has the ability to detect regional differences in myocardium with excellent repeatability, but VFA-based methods have inherent problems with B_1 inhomogeneity, and the long scan time (more than 20 min) makes it impractical to be used in pre- and post-Gd studies. Messroghli et al. acquired myocardial T_1 and ECV maps in rats from a single (unsegmented) dataset using a small animal Look-Locker inversion recovery (SALLI) method [8, 9]. It was able to reconstruct both cine CMR images and T_1 maps, and showed the feasibility to detect diffuse myocardial fibrosis, while the spatial resolution was limited due to signal-to-noise ratio (SNR) consideration. Segmented multi-shot FLASH methods were then proposed to acquire images with higher resolution [10, 11].

In all previous studies with a Look-Locker scheme [12, 13], electrocardiogram (ECG) triggering was used to monitor cardiac motion [8–11]. However, ECG triggering at high field strengths is unreliable due to elevated magnetohydrodynamic effects, which can introduce trigger-related motion artifacts and blurring effects [14, 15]. High heart rates may make the situation even worse. Respiratory navigation was used in some studies [10], however, most studies simply used signal averaging, resulting in image blurring [8, 11]. Furthermore, ECG and respiratory gating setup leads to complicated workflow.

In this study, we developed a ECG-less, free-breathing ECV mapping method using CMR Multitasking [16, 17] (hereinafter abbreviated as *ECV Multitasking*) on a 9.4 T small animal CMR system. It allows continuous acquisition without ECG triggering or respiratory gating. The pre- and post-Gd data were acquired separately but reconstructed jointly, to allow image co-registration and direct ECV mapping. The feasibility of characterizing diffuse myocardial fibrosis was tested in a rat hypertensive heart failure model with preserved ejection fraction (HFpEF), which has been shown to have increased left ventricular (LV) interstitial fibrosis [18–20], and has been recapitulated in recent studies [21–23].

Methods

Animal model

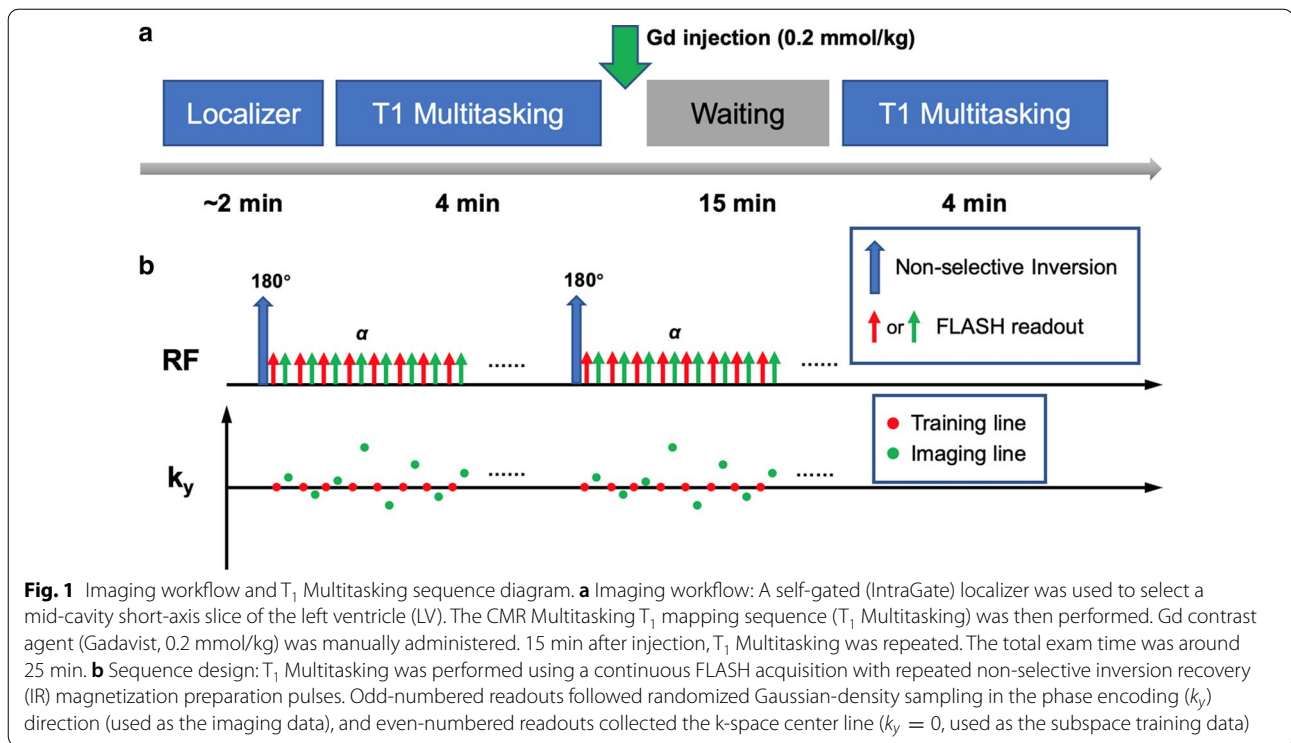
All animal experiments were approved by the Cedars-Sinai Institutional Animal Care and Use Committee. Dahl salt-sensitive (DSS) rats can develop hypertension followed by HFpEF on a high-salt diet [18, 19]. In this model, male DSS rats (Charles River Laboratories, Wilmington, Massachusetts, USA) were normally fed (0.3% NaCl) until the age of 7 weeks. Rats were then randomly assigned to a high-salt (HS) diet group (8% NaCl) to induce HFpEF or a normal-salt (NS) diet group (0.3% NaCl) to serve as controls, until the age of 14 weeks [24]. HS rats with heart failure symptoms (including decreased activity, cachexia, labored breathing, and body edema) and echocardiographic evidence for diastolic dysfunction were diagnosed as HFpEF.

Control rats ($n=9$; weight, 335 ± 44 g) and HS fed rats diagnosed with HFpEF ($n=9$; weight, 286 ± 47 g) were imaged. Imaging experiments and all measurements were done between the age of 14 weeks and 15 weeks. After the imaging study, animals were euthanized, and the hearts were excised. Mid-ventricular heart tissues of the control rats ($n=9$) and HFpEF rats ($n=9$) were sectioned and stained with Masson's trichrome staining.

CMR protocol

All CMR data were acquired on a 9.4 T preclinical system (BioSpec 94/20 USR; Bruker Biospin, Billerica, Massachusetts, USA) using a single-channel volume coil. The T_1 Multitasking sequence was implemented in Paravision 5.1 by modifying the built-in FLASH sequence.

The rat was anesthetized before the scan, and the tail vein was cannulated for later Gd injection within the scan. During the scan, anesthesia was maintained by ventilation



with 1.5% isoflurane-oxygen. After the scan, hematocrit (HCT) level was measured for ECV calculation.

Figure 1a shows the imaging workflow for one rat study. A self-gated (IntraGate) localizer was used to select a slice with a mid-cavity short-axis LV view. The T₁ Multitasking sequence [17] (Fig. 1b) was then performed. Gd contrast agent (Gadavist, 0.2 mmol/kg; Bayer Schering Pharma, Berlin-Wedding, Germany) was manually injected immediately afterwards. Fifteen minutes later, the T₁ Multitasking sequence was repeated on the same slice using identical imaging parameters. The total exam time was ~25 min.

Imaging parameters were: matrix size = 128 × 128, FOV = 40 × 40 mm², voxel size = 0.31 × 0.31 × 1.5 mm³, flip angle = 5°, TR/TE = 7.0/2.4 ms, recovery period (time between adjacent inversion recovery (IR) pulses) = 2.9 s. In each T₁ Multitasking module, 85 IR preparation pulses were applied, resulting in a total scan time of 4 min 10 s.

Data acquired from pre- and post-Gd T₁ Multitasking sequence were reconstructed and analyzed jointly, as described in the following sections. The joint pre- and post-Gd reconstruction can improve respiratory and cardiac binning and promote image co-registration in native and post-Gd T₁ fitting.

Image reconstruction

Images from the proposed ECV Multitasking protocol are represented as a high-dimensional image $A(\mathbf{x}, t_c, t_r, t_{T_1})$

with 2 spatial dimensions and 3 temporal dimensions (cardiac phase t_c , respiratory phase t_r , and T₁ recovery time t_{T_1}). The high-dimensional image can be discretized and viewed as a low-rank tensor \mathcal{A} , and thus partially separable [25], i.e.

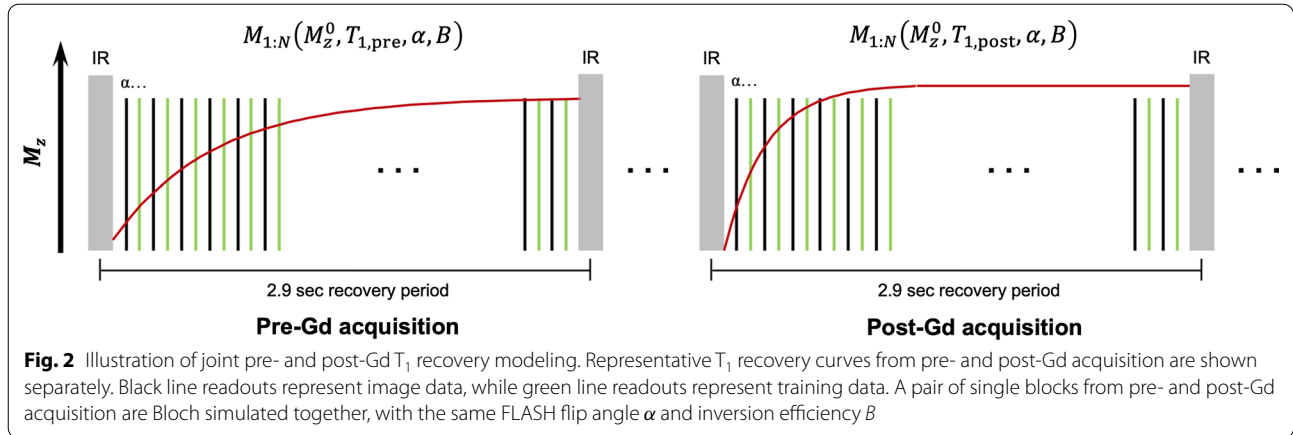
$$\mathbf{A}_{(1)} = \mathbf{U}_x \mathbf{C}_{(1)} (\mathbf{U}_c \otimes \mathbf{U}_r \otimes \mathbf{U}_{T_1})^T \quad (1)$$

where columns of \mathbf{U}_x represents spatial basis functions; columns of \mathbf{U}_c , \mathbf{U}_r , and \mathbf{U}_{T_1} contain cardiac, respiratory, and T₁ recovery temporal basis functions, respectively; \otimes denotes the Kronecker product; and $\mathbf{A}_{(1)}$ and $\mathbf{C}_{(1)}$ are mode-1 matricization of the image tensor \mathcal{A} and the core tensor \mathcal{C} respectively [26].

Equation (1) permits $\mathbf{A}_{(1)} = \mathbf{U}_x \Phi$, where $\Phi = \mathbf{C}_{(1)} (\mathbf{U}_c \otimes \mathbf{U}_r \otimes \mathbf{U}_{T_1})^T$, in which Φ and \mathbf{U}_x contain separate temporal and spatial bases respectively. Therefore, Φ can be first recovered using only the training data \mathbf{d}_{tr} , which is frequently sampled in time, via Bloch-constrained low-rank tensor completion followed by high-order singular value decomposition (HOSVD) [16, 27]. With Φ determined, the spatial basis \mathbf{U}_x can then be reconstructed from the imaging data \mathbf{d}_{im} by solving the following problem:

$$\hat{\mathbf{U}}_x = \arg \min_{\mathbf{U}_x} \|\mathbf{d}_{im} - \Omega(\mathbf{E} \mathbf{U}_x \Phi)\|_2^2 + \lambda R(\mathbf{U}_x) \quad (2)$$

where \mathbf{E} is the signal encoding operator, including Fourier transformation and coil sensitivities weighting (optional),



Ω is the undersampling operator, and R is a regularization functional which was chosen here as a wavelet sparsity penalty in order to additionally exploit compressed sensing [28].

A detailed description of the basic image model and reconstruction scheme used in CMR Multitasking can be found in previous work [16, 17, 29]. In this work, it is divided into the following steps:

Determination of T_1 recovery basis functions in U_{T_1} with Bloch simulation

The inversion recovery (IR)-prepared T_1 recovery process is modeled by Bloch simulations to determine U_{T_1} . In this work, pairs of pre- and post-Gd T_1 recovery curves were jointly simulated as shown in Fig. 2, for the purposes of joint physical modeling during respiratory and cardiac binning (Step 3) and multidimensional image reconstruction (Step 4). The detailed information of the T_1 recovery modeling is available in Appendix.

A dictionary was generated with this model using 101 T_1 values ranging from 100 to 3000 ms ($T_{1,pre} > T_{1,post}$ combinations only), 15 FLASH flip angles from 0.5 to 7.5°, and 21 inversion efficiency values from -1 (complete inversion) to 0 (no inversion). The singular value decomposition (SVD) of this dictionary yielded the T_1 recovery basis functions U_{T_1} .

Real-time image reconstruction

A “real-time” (i.e., ungated before sorting into multiple time dimensions) image was first generated for motion identification:

$$X_{rt} = U_{x,rt} \Phi_{rt} \tag{3}$$

where rows of Φ_{rt} correspond to the real-time temporal basis functions, and columns of $U_{x,rt}$ correspond to the spatial basis functions.

The real-time temporal basis Φ_{rt} was estimated from the SVD of the training data d_{tr} . Then the spatial coefficients $U_{x,rt}$ were recovered by solving the least-squares optimization problem:

$$\hat{U}_{x,rt} = \arg \min_{U_{rt}} \|d_{im} - \Omega(EU_{x,rt} \Phi_{rt})\|_2^2 \tag{4}$$

Respiratory and cardiac binning

Different time points of X_{rt} were assigned to multiple respiratory motion states (“respiratory bins”) and cardiac motion states (“cardiac bins”) based on the real-time images generated in Step 2. A modified k-means clustering method was used to automatically group the data into different bins, incorporating the predetermined low-rank T_1 recovery model in U_{T_1} to address the contrast change of X_{rt} from T_1 recovery [16].

Tensor formation and multidimensional reconstruction

After cardiac and respiratory binning, each readout time point was assigned three temporal indices: cardiac phase, respiratory phase, and T_1 recovery index. A 4-way training data tensor \mathcal{D}_{tr} with one k-space readout dimension and three temporal dimensions was recovered from the subspace training data d_{tr} by solving a Bloch-constrained low-rank tensor completion problem.

After \mathcal{D}_{tr} is completed, the cardiac basis functions U_c , the respiratory basis functions U_r , and the core tensor \mathcal{C} can be extracted from the HOSVD of \mathcal{D}_{tr} , fully determining $\Phi = \mathcal{C}_{(1)}(U_c \otimes U_r \otimes U_{T_1})^T$. The spatial coefficients U_x can then be reconstructed by solving the problem in Eq. (2).

Parameter fitting and image analysis

One specific respiratory phase and cardiac phase were selected for T_1 and ECV map generation, corresponding

to end-expiration and end-diastole respectively. A joint pre- and post-Gd T_1 recovery model was also used in pixel-wise T_1 fitting. By fitting this joint model (see Appendix), we can get the pre- and post-Gd T_1 maps simultaneously.

Myocardial T_1 maps

Parameter fitting was done using the joint pre- and post-Gd T_1 recovery model in Eq. (11). $T_{1,pre}$, $T_{1,post}$, α , B , and M_z^0 were fitted using the 832 inversion time images at the selected reparatory and cardiac phase. The pre- and post-Gd myocardial T_1 maps were directly generated from the $T_{1,pre}$ and $T_{1,post}$ fitting results.

Blood T_1 fitting

First, the pixels to be used for blood T_1 fitting were automatically selected based on the thresholding of the fitted M_z^0 map. Then, the average T_1 recovery curve from these pixels was calculated, weighted by the M_z^0 map. Finally, parameters were fitted to the average blood T_1 recovery curves using the model in Eq. (11) without Look-Locker correction (i.e., with $M_n(M_z^0, T_1, \alpha = 0, B)$) to better model the inflow of unexcited blood spins into the imaging slice [17]. The fitted $T_{1,pre}$ and $T_{1,post}$ values were then used as the pre- and post-Gd blood T_1 values.

ECV calculation

The ECV map was generated according to the following equations:

$$ECV = (1 - HCT) \cdot \frac{\Delta R_{1,myo}}{\Delta R_{1,blo}} \times 100\% \tag{5}$$

$$\Delta R_1 = R_{1,post} - R_{1,pre} = \frac{1}{T_{1,post}} - \frac{1}{T_{1,pre}} \tag{6}$$

in which $\Delta R_{1,myo}$ is the pixel-wise R_1 changes, and $\Delta R_{1,blo}$ is the change of blood R_1 , and HCT is the hematocrit value. All statistical analyses were performed for septal ECV, i.e., where $\Delta R_{1,myo}$ was calculated as the mean value within the septal myocardium. All image reconstruction and curve fitting was done in MATLAB 2018a (MathWorks, Natick, Massachusetts, USA).

Phantom validation

The accuracy of T_1 fitting of the pre- or post-Gd T_1 Multitasking sequence was tested in an 8-vial water phantoms with $GdCl_3$ concentrations of 0, 10, 20, 33, 50, 80, 120 and 200 $\mu\text{mol/kg}$. T_1 maps generated by the Bruker built-in RARE-VTR method was used as the reference. The imaging parameters of RARE-VTR were: TE=19.5 ms, TR array=8000, 4000, 1500, 800, 400, 200 and 120 ms,

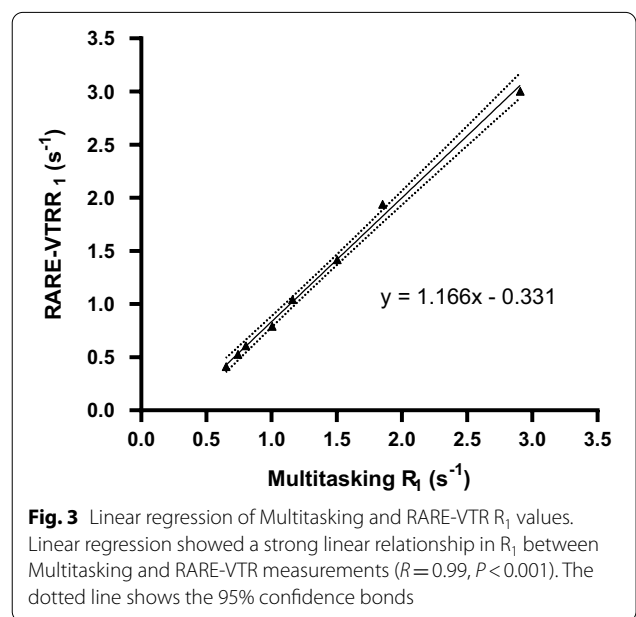
RARE factor=4, matrix size=128 × 128, FOV=40 × 40 mm^2 , and total scan time=6 min 1 s.

Histological analysis

Masson’s trichrome staining was used to measure the extent of fibrosis. Mid-ventricular heart tissues were sectioned and stained following the manufacturer’s protocol (Sigma-Aldrich, St. Louis, Missouri, USA). Quantitative histological analysis was done with ImageJ 1.52a (National Institutes of Health; <http://imagej.nih.gov/ij>). In each section, the extent of myocardial fibrosis was quantified by the percentage of total fibrosis area, which was calculated as the number of blue-stained pixels divided by the total number of pixels in the ventricular area (excluded: intramural vascular structures, perivascular collagen, endocardium, and LV trabeculae) [20, 30]. For each rat, the average percentage from five different sections was reported.

Statistical analysis

Welch’s t-test was performed to compare ECV values between the control group and HFpEF group. The Pearson coefficient was measured to evaluate the correlation between ECV values and quantitative fibrosis percentages. A two-tailed value of $P < 0.05$ was considered to be statistically significant. Statistical graphs were generated using GraphPad Prism 8 (GraphPad Software, San Diego, California, USA) and Excel (Microsoft Corporation, Redmond, Washington, USA).



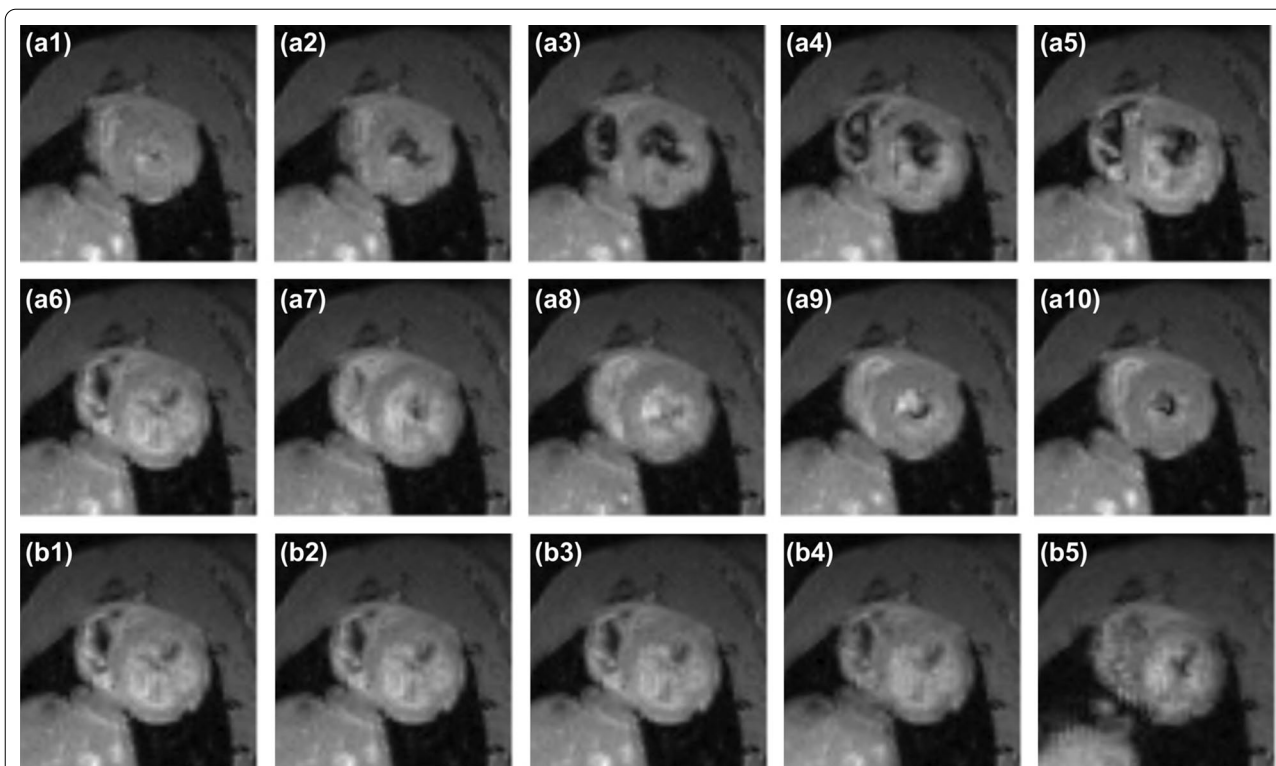


Fig. 4 Images of different cardiac and respiratory bins. Representative images of **a** ten different cardiac bins (a1–a10), and **b** five different respiratory bins (b1–b5) at the beginning of an inversion recovery preparation pulse. Movies are available in Additional file 1, showing the dynamic images from (1) different respiratory bins, (2) different cardiac bins, (3) native T_1 recovery process, and (4) post-Gd T_1 recovery process

Results

The reference T_1 of the phantoms measured by RARE-VTR ranged from 333 to 2433 ms, with a corresponding R_1 range from 0.41 to 3.00 s^{-1} . Figure 3 shows the linear regression result of R_1 values measured by Multitasking and RARE-VTR, in which a strong linear relationship can be found ($R = 0.9983, P < 0.0001$).

Five respiratory bins and ten cardiac bins were used for respiratory and cardiac binning, corresponding to a cardiac temporal resolution of 20 ms for a heart rate of ~300 bpm. Figure 4 shows the images of the heart from a representative healthy control rat right before the IR preparation pulse, generated from different cardiac and respiratory phases, i.e. $\mathcal{A}(x, n_c, n_r, n_{T_1})|_{n_c=1:10, n_r=1, n_{T_1}=N=416}$ (Fig. 4a) and $\mathcal{A}(x, n_c, n_r, n_{T_1})|_{n_c=6, n_r=1:5, n_{T_1}=N=416}$ (Fig. 4b). The diastole (Fig. 4a6) and the systole (Fig. 4a1), or the end-expiration phase (Fig. 4b1) and the end-inspiration phase (Fig. 4b5) can be clearly differentiated in the figure. Movies showing the dynamic images from (1) different respiratory bins, (2) different cardiac bins, (3) native T_1 recovery process, and (4) post-Gd T_1 recovery process are also available in Additional file 1.

Figure 5a, b shows representative native and post-Gd T_1 maps from the control group and heart failure with preserved ejection fraction (HFpEF) group. T_1 maps were smooth and homogeneous within the left ventricular (LV) myocardium, except for areas in the inferior and lateral walls with imperfect fitting results (as indicated by white arrows in Fig. 5a1, a2). The native myocardial T_1 values (mean \pm SD, in ms) were 1662 ± 152 in the HFpEF group (vs 1534 ± 151 in the control group; $P = 0.09$). Figure 5c shows the corresponding ECV maps. In this study, signal from the aorta rather than the LV was usually selected for blood T_1 fitting, because of the signal loss resulting from LV inflow in this single slice setup; and the septal myocardium areas selected for $\Delta R_{1, \text{myo}}$ calculation were indicated by red arrows. Welch’s t-test showed that ECV was significantly higher in the HFpEF group ($22.4\% \pm 2.5\%$ vs. $18.0\% \pm 2.1\%$; $P = 0.0010$, Fig. 5d).

In eight rats (4 control + 4 HFpEF), an additional post-Gd T_1 Multitasking sequence was run 10 min after the Gd injection, with identical imaging parameters. ECVs were also calculated using this separate post-Gd T_1 measurement. Figure 6 shows the Bland–Altman plot comparing the ECVs measured from the 15-min post-Gd T_1 (ECV_{15}) and the 10-min post-Gd T_1 (ECV_{10}). The

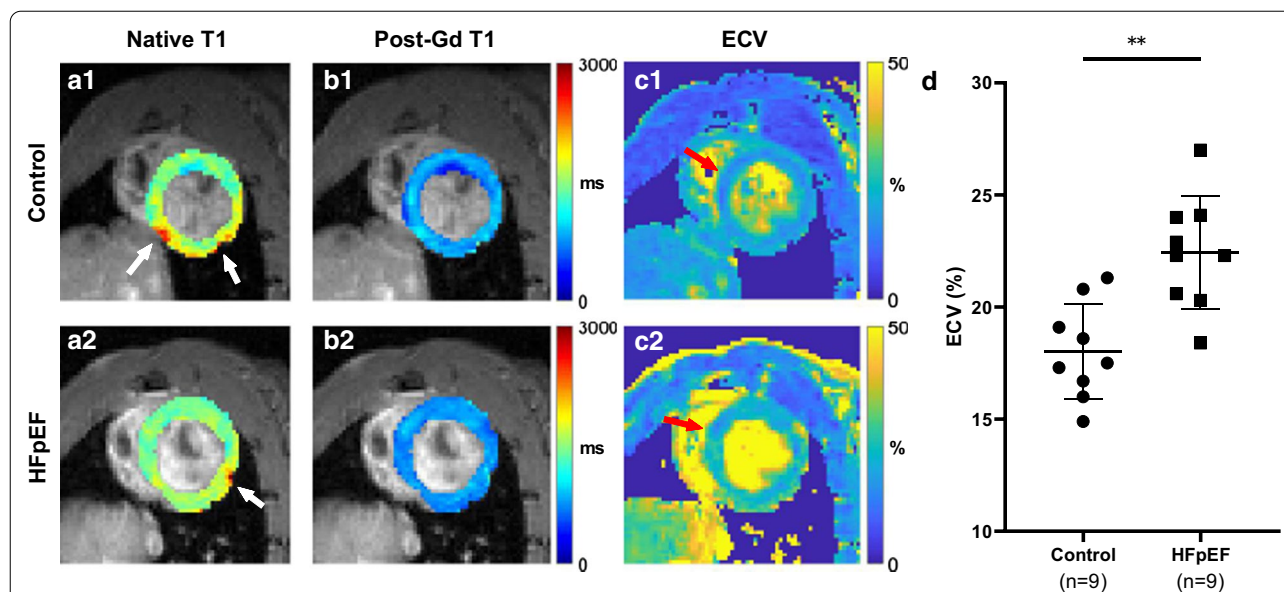


Fig. 5 Representative T₁ and Extracellular volume fraction (ECV) maps (local) from the control and heart failure with preserved ejection fraction (HFpEF) group. **a–c** Representative T₁ and ECV maps from the control group (1) and HFpEF group (2). Myocardial R₁ changes for the final ECV analysis were calculated within septal myocardium, as indicated by red arrows in **c**. **d** ECV values were significantly higher in HFpEF group (22.43% ± 2.51%), compared with the control group (18.02% ± 2.13%), *P* = 0.0010

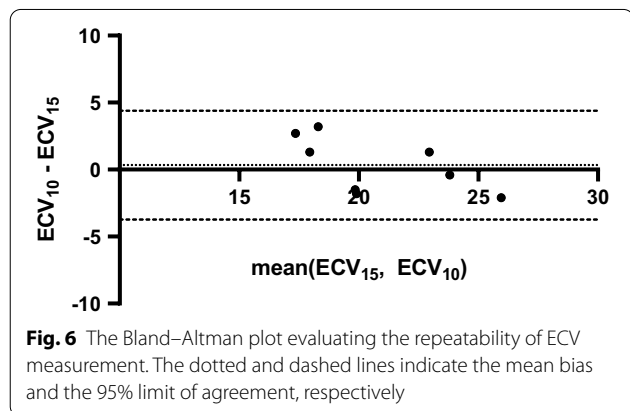


Fig. 6 The Bland–Altman plot evaluating the repeatability of ECV measurement. The dotted and dashed lines indicate the mean bias and the 95% limit of agreement, respectively

interclass correlation coefficient (ICC) was 0.817. The root-mean-square within-subject standard deviation was 1.4, yielding a coefficient of variation of 6.7%. There was no significant difference between ECV₁₅ and ECV₁₀ (*P* = 0.66).

Figure 7a, b shows representative Masson trichrome-stained sections of a HFpEF and control rat. The myocardial fibrosis can be clearly seen as the diffused dark blue areas in Fig. 7b. The extent of fibrosis significantly increased in HFpEF hearts (11.7% ± 1.9% vs 3.4% ± 0.8%, *P* < 0.001) Fig. 7c shows the relationship between the ECV value and the extent of fibrosis, in which a moderate correlation can be found (*R* = 0.59, *P* = 0.0098).

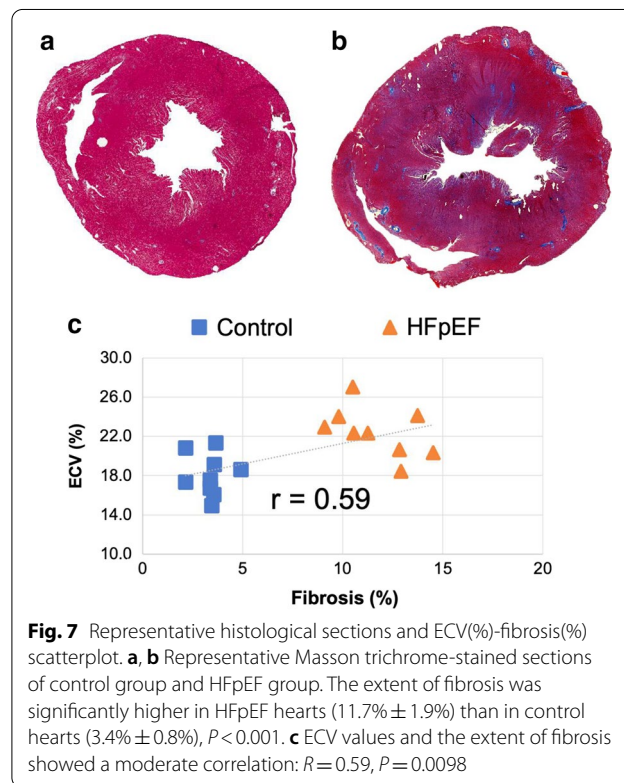


Fig. 7 Representative histological sections and ECV(%)–fibrosis(%) scatterplot. **a, b** Representative Masson trichrome-stained sections of control group and HFpEF group. The extent of fibrosis was significantly higher in HFpEF hearts (11.7% ± 1.9%) than in control hearts (3.4% ± 0.8%), *P* < 0.001. **c** ECV values and the extent of fibrosis showed a moderate correlation: *R* = 0.59, *P* = 0.0098

Discussion

We developed a novel ECV Multitasking protocol which can map ECV at high heart rates without ECG triggering

or respiratory navigation. To test its feasibility to characterize diffuse myocardial fibrosis, a HFpEF rat model was chosen in this study. Although ECV has not previously been measured in a HFpEF rat model, there has been increasing clinical interest in T_1 and ECV characterization of patients with HFpEF in recent years. Several publications showed elevated ECV in HFpEF patients versus control subjects. Su et al. reported that patients with HFpEF had elevated ECV compared with control subjects (28.9% vs. 27.9%, $P=0.006$) [6]. Rommel et al. reported similar results (32.9% vs. 28.9%, $P<0.01$) [5], and Mordi et al. also confirmed this finding (35.9% vs. 27.0%, $P<0.001$) [4]. A modified Look-Locker inversion recovery (MOLLI) sequence was used to perform T_1 mapping in all of these studies. In the present study, ECV characterization was performed for the first time in a HFpEF rat model. The elevated ECV we found with HFpEF (22.4% vs. 18.0%, $P=0.001$) is consistent with previous human studies. Though so far only tested in the DSS rat model for HFpEF diagnosis [18, 19], this newly developed technique can easily be extended to other small animal applications. More importantly, the non-invasive quantitative imaging protocol not only provides a diagnostic tool, but also a method for longitudinal therapy monitoring of the same subject [31].

In the control group, native T_1 values were 1534 ± 151 ms and ECV values were $18.0\% \pm 2.1\%$ (both calculated from the septal area). Previous rodent studies have reported variable myocardial T_1 values, depending on field strength and T_1 encoding schemes, both of which are known to affect T_1 estimates. At 7.0 T, T_1 values were reported as 1620 ms (Vandsburger et al.) and 1638 ms (Zhang et al.) [10, 32]. At 9.4 T, reported T_1 values ranged from ~ 1200 ms to 1764 ms (Kim et al. Li et al. and Coolen et al.) [7, 33, 34]. ECV, a physiological quantity in principle unaffected by field strength or T_1 encoding scheme, allows more direct comparison. In healthy rats, myocardial ECV was previously reported as 16% [35], 18% [36], 17.2% [9], and 15.5% [34], comparable with the 18.0% value measured in our study. A direct comparison to these previous methods on the same scanner and in the same subjects was not performed in the present study, but would be a useful future validation step.

One major technical novelty of this work compared with previous CMR Multitasking work is the joint reconstruction of pre- and post-Gd data and the paired modeling of the pre- and post-Gd T_1 recovery. This has two primary benefits. First, it allows the respiratory and cardiac binning to be done in the concatenated pre- and post-Gd data. In this way, the data with a similar motion state—no matter whether from pre-Gd or post-Gd—will be clustered into exactly the same respiratory or cardiac bin, removing the need for respiratory co-registration

between pre- and post-Gd T_1 maps. Second, it can improve the robustness of T_1 fitting by constraining pre- and post-Gd images to share the same thermal equilibrium magnetization M_z^0 , FLASH flip angle α and inversion efficiency B , exploiting internal a priori knowledge and reducing the total number of fitting parameters from 8 to 5.

The phantom study found that the Multitasking based T_1 fitting results showed a strong linear correlation with the RARE-VTR reference. If calibrated using the linear correlation ($R_1 = LC(R_1) = 1.166R_1 - 0.331$), the relative R_1 difference between Multitasking method and RARE-VTR reference would be $2.7\% \pm 3.6\%$. Note that ECV measurements are insensitive to linear transformation: the ECV value is calculated by the ratio of R_1 changes of myocardial and blood pool, so both the intercept (-0.331) and slope (1.166) of the linear transformation LC will be canceled, leaving the final ECV quantification result unchanged.

Ten bins were used to separate different cardiac phases in the current protocol for CMR ECV Multitasking reconstruction, corresponding to a cardiac temporal resolution of 20 ms for a heart rate of 300 bpm. As shown in Fig. 2, the diastolic and systolic phases can be differentiated at this temporal resolution. However, for higher heart rates, such as those in mice (around 450 bpm), more cardiac bins may be required, which may have an impact on SNR and ECV homogeneity. A nearly-significant negative correlation ($R = -0.44$, $P = 0.06$) was found between the septal SNR of the ECV map and the heart rate (the scatterplot can be found in Additional file 1). This may be an effect of increased intra-bin motion at higher heart rates. More cardiac bins can possibly be achieved by shortening the echo spacing, or by acquiring k-space training line and imaging lines in separate echoes after each FLASH flip angle [37].

In this work, blood T_1 was extracted by fitting the weighted average T_1 recovery curve of the selected blood pool. The FLASH flip angle α in Eq. (8) was fixed as 0 to remove Look-Locker correction and better model the inflow of unexcited blood spins. This approach is particular to 2D slice-selective excitation, for which blood spins flow through the slice quickly enough that Look-Locker correction is not required. For a volumetric 3D variation of our method, the blood spins would be driven towards steady-state, and the Look-Locker correction could be retained in blood.

T_1 inhomogeneity was present in the inferior and lateral walls due to potential B_1 issues at high B_0 field, as visible in Fig. 4. In diffuse myocardial disease, it does not affect the ECV calculation from septal area. However, it will affect the accuracy of the ECV map in the inferior and lateral walls. This may reduce the reliability of

the method in the diagnosis of focal myocardial disease, such as focal myocardial infarction. Further sequence improvements, such as a dual-flip-angle acquisition [38], should be made to address this problem.

The method described here did not include bulk motion compensation, as anesthesia and additional immobilization setup did not result in any apparent bulk motion. However, bulk motion compensation is compatible with the CMR Multitasking framework, as described in [39], where a translational inter-bin registration to k-space data was applied prior to joint reconstruction. Similar motion compensation could be incorporated into the proposed method if used with different experimental setups more susceptible to bulk motion.

Currently, a total of 85 IR preparation pulses were applied in each T_1 Multitasking module, resulting in a single-slice scan of just over 4 min. However, the minimum required scan time was not systematically explored, so further shortening of the scan time may yet be possible.

Future work will include optimizing the number of cardiac bins, expanding spatial coverage with 3D volumetric imaging, as well as addressing B_1 and B_0 issues affecting T_1 homogeneity in the inferior and lateral walls. Further imaging tests will also include using ECV Multitasking for longitudinal therapy monitoring, such as the cardiosphere-derived cell (CDC) treatment of HFpEF [31].

Conclusions

We developed an ECG-less, free-breathing CMR Multitasking ECV mapping method at high heart rates. The pre- and post-Gd data were concatenated and reconstructed using a joint T_1 recovery model to generate ECV maps. Elevated ECV found in the HFpEF group agrees well with previous human studies and shows a moderate correlation with the histological data. This technique can serve as a viable CMR imaging tool for myocardial tissue characterization in small animal models.

Supplementary Information

The online version contains supplementary material available at <https://doi.org/10.1186/s12968-020-00699-9>.

Additional file 1: Page 1. The four videos show reconstructed results of (1) steady-state images from five respiratory bins, (2) steady-state images from ten cardiac bins, (3) native inversion recovery process, and (4) post-Gd inversion recovery, respectively. **Page 2:** The scatterplot between the SNR of the ECV map and the heart rate. The SNR was measured as mean/std of the ECV map within the septal area. A nearly-significant negative correlation ($R = -0.44$, $P = 0.06$) can be found between the SNR and the heart rate.

Abbreviations

CDC: Cardiosphere-derived cell; CMR: Cardiovascular magnetic resonance; DSS: Dahl salt-sensitive; ECG: Electrocardiogram; ECV: Extracellular volume fraction; FLASH: Fast low angle shot; HCT: Hematocrit; HFpEF: Heart failure with preserved ejection fraction; HOSVD: High-order singular value decomposition; HS: High salt; IR: Inversion recovery; LV: Left ventricle/left ventricular; MOLLI: Modified Look-Locker inversion recovery; NS: Normal salt; RARE: Rapid acquisition with relaxation enhancement; SALLI: Small animal Look-Locker inversion recovery; SNR: Signal-to-noise ratio; SVD: Singular value decomposition; VFA: Variable flip angle.

Acknowledgements

Not applicable.

Authors' contributions

PH, AC and DL conceived the study. RZ developed the animal model. PH and RZ performed data acquisition. PH implemented the method, performed statistical analysis and drafted the manuscript. SW, YX, AC and DL assisted with the study design. EC and EM supported the animal studies. SW, YX, EC, EM, AC and DL provided critical review of the manuscript. All authors read and approved the final manuscript.

Funding

This work was supported in part by grant from the National Institutes of Health (Grant No. NIH R01 EB028146).

Availability of data and materials

The datasets acquired and/or analyzed during the current study are not publicly available but are available from the corresponding author on reasonable request.

Ethics approval and consent to participate

The protocol was approved by the local Institutional Animal Care and Usage Committee (IACUC) at Cedars-Sinai Medical Center.

Consent for publication

Not applicable.

Competing interests

The authors declare that they have no competing interests.

Author details

¹ Department of Bioengineering, University of California, Los Angeles, Los Angeles, CA, USA. ² Biomedical Imaging Research Institute, Cedars-Sinai Medical Center, Los Angeles, CA, USA. ³ Smidt Heart Institute, Cedars-Sinai Medical Center, Los Angeles, CA, USA. ⁴ Department of Cardiology, Xinhua Hospital Affiliated to Shanghai Jiaotong University School of Medicine, Shanghai, China.

Appendix: T_1 recovery modelling

The z -magnetization within a single recovery period between two adjacent inversion recovery (IR) pulses can be described as

$$M_n = M_{ss} + (BM_{N+1} - M_{ss}) \cdot E^{n-1} \tag{7}$$

$$E = e^{-\frac{TR}{T_1} \cos\alpha}, \tag{8}$$

$$M_{N+1} = M_{ss} \frac{1 - E^N}{1 - BE^N}, \tag{9}$$

where n is the readout index within each recovery period, $n = 1, 2, \dots, N$; $M_{ss} = \frac{1 - e^{-TR/T_1}}{1 - e^{-TR/T_1} \cos\alpha} M_z^0$ is the

z-magnetization at true steady-state ($t \rightarrow \infty$); M_{N+1} is the actual final z-magnetization in each recovery period incorporating incomplete relaxation; and $B \in [-1,0]$ represents the inversion efficiency of the IR pulse. Our pulse sequence used $N = 416$, $TR = 7$ ms; α was prescribed as 5° but was not assumed to be perfectly homogenous during Bloch simulations and during fitting.

Combining Eqs. 7, 8, 9 yields the combined z-magnetization equation

$$M_n(M_z^0, T_1, \alpha, B) = M_{ss}(M_z^0, T_1, \alpha) \cdot \left[1 + \left(B \frac{1 - e^{-\frac{TR}{T_1}} \cos \alpha}{1 - B e^{-\frac{TR}{T_1}} \cos \alpha} - 1 \right) \cdot \left(e^{-\frac{TR}{T_1}} \cos \alpha \right)^{n-1} \right] \quad (10)$$

Assuming that the B_1 field does not change between pre- and post-contrast acquisitions, the unknown actual FLASH flip angle α and inversion efficiency B can be assumed to be constant for each pixel. Therefore the paired signal model concatenating the pre- and post-Gd signal evolution is:

$$S(M_z^0, T_{1,pre}, T_{1,post}, \alpha, B) = \left\{ M_{1:N}(M_z^0, T_{1,pre}, \alpha, B), M_{1:N}(M_z^0, T_{1,post}, \alpha, B) \right\} \cdot \sin \alpha \quad (11)$$

Received: 5 April 2020 Accepted: 10 December 2020
Published online: 11 February 2021

References

1. Moon JC, Messroghli DR, Kellman P, Piechnik SK, Robson MD, Ugander M, Gatehouse PD, Arai AE, Friedrich MG, Neubauer S, Schulz-Menger J. Myocardial T1 mapping and extracellular volume quantification: A Society for Cardiovascular Magnetic Resonance (SCMR) and CMR Working Group of the European Society of Cardiology consensus statement. *J Cardiovasc Magn Reson*. 2013;15(1):92.
2. Puntmann VO, Peker E, Chandrashekar Y, Nagel E. T1 mapping in characterizing myocardial disease: a comprehensive review. *Circ Res*. 2016;119(2):277–99.
3. Haaf P, Garg P, Messroghli DR, Broadbent DA, Greenwood JP, Plein S. Cardiac T1 mapping and extracellular volume (ECV) in clinical practice: a comprehensive review. *J Cardiovasc Magn Reson*. 2017;18(1):89.
4. Mordi IR, Singh S, Rudd A, Srinivasan J, Frenneaux M, Tzemos N, Dawson DK. Comprehensive echocardiographic and cardiac magnetic resonance evaluation differentiates among heart failure with preserved ejection fraction patients, hypertensive patients, and healthy control subjects. *JACC Cardiovasc Imaging*. 2017;16:2344.
5. Rommel KP, von Roeder M, Latuscynski K, Oberueck C, Blazek S, Fengler K, Besler C, Sandri M, Lücke C, Gutberlet M, Linke A. Extracellular volume fraction for characterization of patients with heart failure and preserved ejection fraction. *J Am Coll Cardiol*. 2016;67(15):1815–25.
6. Su MY, Lin LY, Tseng YH, Chang CC, Wu CK, Lin JL, Tseng WY. CMR-verified diffuse myocardial fibrosis is associated with diastolic dysfunction in HFpEF. *JACC Cardiovasc Imaging*. 2014;7(10):991–7.
7. Coolen BF, Geelen T, Paulis LE, Nauerth A, Nicolay K, Strijkers GJ. Three-dimensional T1 mapping of the mouse heart using variable flip angle steady-state MR imaging. *NMR Biomed*. 2011;24(2):154–62.
8. Messroghli DR, Nordmeyer S, Buehrer M, Kozerke S, Dietrich T, Kaschima E, Becher PM, Hucko T, Berger F, Klein C, Kuehne T. Small animal Look-Locker Inversion Recovery (SALLI) for simultaneous generation of cardiac T1

- maps and cine and inversion recovery-prepared images at high heart rates: initial experience. *Radiology*. 2011;261(1):258–65.
9. Messroghli DR, Nordmeyer S, Dietrich T, Dirsch O, Kaschima E, Savvatis K, Oh-Ici D, Klein C, Berger F, Kuehne T. Assessment of diffuse myocardial fibrosis in rats using small-animal Look-Locker inversion recovery T1 mapping. *Circulation*. 2011;4(6):636–40.
10. Zhang H, Ye Q, Zheng J, Schelbert EB, Hitchens TK, Ho C. Improve myocardial T1 measurement in rats with a new regression model: application to myocardial infarction and beyond. *Magn Reson Med*. 2014;72(3):737–48.
11. Smit H, Guridi RP, Guenoun J, Poot DH, Doeswijk GN, Milanese M, Bernsen MR, Krestin GP, Klein S, Kotek G. T1 mapping in the rat myocardium at 7 tesla using a modified CINE inversion recovery sequence. *J Magn Reson*

- Imaging. 2014;39(4):901–10.
12. Look DC, Locker DR. Time saving in measurement of NMR and EPR relaxation times. *Rev Sci Instrum*. 1970;41(2):250–1.
13. Messroghli DR, Radjenovic A, Kozerke S, Higgins DM, Sivananthan MU, Ridgway JP. Modified Look-Locker inversion recovery (MOLLI) for high-resolution T1 mapping of the heart. *Magn Reson Med*. 2004;52(1):141–6.
14. Ståb D, Roessler J, O'Brien K, Hamilton-Craig C, Barth M. ECG triggering in

- ultra-high field cardiovascular MRI. *Tomography*. 2016;2(3):167.
15. Krug JW, Rose G, Clifford GD, Oster J. ECG-based gating in ultra high field cardiovascular magnetic resonance using an independent component analysis approach. *J Cardiovasc Magn Reson*. 2013;15(1):104.
16. Christodoulou AG, Shaw JL, Nguyen C, Yang Q, Xie Y, Wang N, Li D. Magnetic resonance multitasking for motion-resolved quantitative cardiovascular imaging. *Nat Biomed Eng*. 2018;2(4):215.
17. Shaw JL, Yang Q, Zhou Z, Deng Z, Nguyen C, Li D, Christodoulou AG. Free-breathing, non-ECG, continuous myocardial T1 mapping with cardiovascular magnetic resonance multitasking. *Magn Reson Med*. 2019;81(4):2450–63.
18. Doi R, Masuyama T, Yamamoto K, Doi Y, Mano T, Sakata Y, Ono K, Kuzuya T, Hirota S, Koyama T, Miwa T. Development of different phenotypes of hypertensive heart failure: systolic versus diastolic failure in Dahl salt-sensitive rats. *J Hypertension*. 2000;18(1):111–20.
19. Klotz S, Hay I, Zhang G, Maurer M, Wang J, Burkhoff D. Development of heart failure in chronic hypertensive Dahl rats: focus on heart failure with preserved ejection fraction. *Hypertension*. 2006;47(5):901–11.
20. Cho JH, Zhang R, Kilfoil PJ, Gallet R, de Couto G, Bresee C, Goldhaber JI, Marbán E, Cingolani E. Delayed repolarization underlies ventricular arrhythmias in rats with heart failure and preserved ejection fraction. *Circulation*. 2017;136(21):2037–50.
21. Hogg K, Swedberg K, McMurray J. Heart failure with preserved left ventricular systolic function: epidemiology, clinical characteristics, and prognosis. *J Am Coll Cardiol*. 2004;43(3):317–27.
22. Owan TE, Hodge DO, Herges RM, Jacobsen SJ, Roger VL, Redfield MM. Trends in prevalence and outcome of heart failure with preserved ejection fraction. *N Engl J Med*. 2006;355(3):251–9.
23. Shah KS, Xu H, Matsuoka RA, Bhatt DL, Heidenreich PA, Hernandez AF, Devore AD, Yancy CW, Fonarow GC. Heart failure with preserved, borderline, and reduced ejection fraction: 5-year outcomes. *J Am Coll Cardiol*. 2017;70(20):2476–86.
24. Gallet R, de Couto G, Simsolo E, Valle J, Sun B, Liu W, Tseliou E, Zile MR, Marbán E. Cardiosphere-derived cells reverse heart failure with preserved ejection fraction in rats by decreasing fibrosis and inflammation. *JACC*. 2016;1(1–2):14–28.
25. Liang ZP. Spatiotemporal imaging with partially separable functions. In: 2007 4th IEEE International Symposium on Biomedical Imaging: From Nano to Macro 2007 Apr 12 (pp. 988–991). IEEE.

26. Kolda TG, Bader BW. Tensor decompositions and applications. *SIAM Rev.* 2009;51(3):455–500.
27. De Lathauwer L, De Moor B, Vandewalle J. A multilinear singular value decomposition. *SIAM J Matrix Anal Appl.* 2000;21(4):1253–78.
28. Lustig M, Donoho D, Pauly JM. Sparse MRI: the application of compressed sensing for rapid MR imaging. *Magn Reson Med.* 2007;58(6):1182–95.
29. Wang N, Christodoulou AG, Xie Y, Wang Z, Deng Z, Zhou B, Lee S, Fan Z, Chang H, Yu W, Li D. Quantitative 3D dynamic contrast-enhanced (DCE) MR imaging of carotid vessel wall by fast T1 mapping using Multitasking. *Magn Reson Med.* 2019;81(4):2302–14.
30. Wolf CM, Moskowitz IP, Arno S, Branco DM, Semsarian C, Bernstein SA, Peterson M, Maida M, Morley GE, Fishman G, Berul CI. Somatic events modify hypertrophic cardiomyopathy pathology and link hypertrophy to arrhythmia. *Proc Natl Acad Sci USA.* 2005;102(50):18123–8.
31. Grigorian-Shamagian L, Liu W, Fereydooni S, Middleton RC, Valle J, Cho JH, Marbán E. Cardiac and systemic rejuvenation after cardiosphere-derived cell therapy in senescent rats. *Eur Heart J.* 2017;38(39):2957–67.
32. Vandsburger MH, Janiczek RL, Xu Y, French BA, Meyer CH, Kramer CM, Epstein FH. Improved arterial spin labeling after myocardial infarction in mice using cardiac and respiratory gated look-locker imaging with fuzzy C-means clustering. *Magn Reson Med.* 2010;63(3):648–57.
33. Li W, Griswold M, Yu X. Rapid T1 mapping of mouse myocardium with saturation recovery look-locker method. *Magn Reson Med.* 2010;64(5):1296–303.
34. Kim PK, Hong YJ, Sakuma H, Chawla A, Park JK, Park CH, Hong D, Han K, Lee JY, Hur J, Lee HJ. Myocardial extracellular volume fraction and change in hematocrit level: MR evaluation by using T1 mapping in an experimental model of anemia. *Radiology.* 2018;288(1):93–8.
35. Arheden H, Saeed M, Higgins CB, Gao DW, Bremerich J, Wyttenbach R, Dae MW, Wendland MF. Measurement of the distribution volume of gadopentetate dimeglumine at echo-planar MR imaging to quantify myocardial infarction: comparison with 99mTc-DTPA autoradiography in rats. *Radiology.* 1999;211(3):698–708.
36. Arheden H, Saeed M, Higgins CB, Gao DW, Ursell PC, Bremerich J, Wyttenbach R, Dae MW, Wendland MF. Reperfused rat myocardium subjected to various durations of ischemia: estimation of the distribution volume of contrast material with echo-planar MR imaging. *Radiology.* 2000;215(2):520–8.
37. Christodoulou AG, Wu YL, Hitchens TK, Ho C, Liang ZP. Self-navigated low-rank MRI for MPIO-labeled immune cell imaging of the heart. In 2014 36th Annual International Conference of the IEEE Engineering in Medicine and Biology Society 2014 Aug 26 (pp. 1529–1532). IEEE.
38. Serry FM, Ma S, Li D, Christodoulou AG. Dual flip-angle IR-FLASH for B1+ insensitive T1 mapping: Application to T1 CMR Multitasking. In Proceedings of the 2020 ISMRM & SMRT Virtual Conference and Exhibition. p. 0895.
39. Wang N, Gaddam S, Wang L, Xie Y, Fan Z, Yang W, Tuli R, Lo S, Hendifar A, Pandol S, Christodoulou AG. Six-dimensional quantitative DCE MR Multitasking of the entire abdomen: Method and application to pancreatic ductal adenocarcinoma. *Magn Reson Med.* 2020;84(2):928–48.

Publisher's Note

Springer Nature remains neutral with regard to jurisdictional claims in published maps and institutional affiliations.

Ready to submit your research? Choose BMC and benefit from:

- fast, convenient online submission
- thorough peer review by experienced researchers in your field
- rapid publication on acceptance
- support for research data, including large and complex data types
- gold Open Access which fosters wider collaboration and increased citations
- maximum visibility for your research: over 100M website views per year

At BMC, research is always in progress.

Learn more biomedcentral.com/submissions

